Research Article Vol. 31, No. 18 / 28 Aug 2023 / Optics Express 29515
Optics EXPRESS

Emulating the Deutsch-Josza algorithm with an inverse-designed terahertz gradient-index lens

ASHLEY N. BLACKWELL, RIAD YAHIAOUI, YI-HUAN CHEN, PAI-YEN CHEN, THOMAS A. SEARLES, AND ZIZWE A. CHASE*

Electrical & Computer Engineering, University of Illinois Chicago, Chicago, IL 60607, USA
chase8@uic.edu

Abstract: An all-dielectric photonic metastructure is investigated for application as a quantum algorithm emulator (QAE) in the terahertz frequency regime; specifically, we show implementation of the Deustsh-Josza algorithm. The design for the QAE consists of a gradient-index (GRIN) lens as the Fourier transform subblock and patterned silicon as the oracle subblock. First, we detail optimization of the GRIN lens through numerical analysis. Then, we employed inverse design through a machine learning approach to further optimize the structural geometry. Through this optimization, we enhance the interaction of the incident light with the metamaterial via spectral improvements of the outgoing wave.

1. Introduction

Improvement upon current computing architecture is required in order to enhance computation power, time and resources for industries such as medicine, catalysis, and finance. As compared to digital computers, optical computers offer the capabilities of parallel processing, high speed, lower power consumption, and operation at multiple frequencies [1,2] thus exploiting a photonic system can make these devices a prime candidate to realize this possibility [3], especially in the least exploited THz regime. In order to achieve an integrated analog optical computing system, it is necessary to focus the incident wave to the next operational computing component which can be achieved by the use of computational metamaterials. Numerous systems, designed for free space, have been proposed but have been difficult to integrate and bulky in design [4–7]. One such metamaterial known as the gradient index (GRIN) lens, can alleviate these issues through being an on-chip device. A prototypical GRIN lens consists of a series of micro-layered structures with holes of different geometries to vary the index of refraction [8,9] that manipulate the propagation of electromagnetic waves [10]. Previous works of GRIN lens metamaterial structures have theoretically and experimentally demonstrated to operate in the THz regime [11–13] with strong focusing capabilities [14–16] and tunability [17–19].

Recently, GRIN lenses have been integrated as components of larger photonic devices, consisting of a multitude of subblocks, to realize a new optical computing technology, the quantum algorithm emulator (QAE). QAEs simulate quantum search algorithms with classical waves via the superposition principle and interference phenomena which is integral to rapid searching and solving difficult problems that would be time and power consuming on digital computers [4,20,21]. QAEs have only been explored in the microwave region where the measured electric field amplitude is the probability amplitude of the equivalent quantum state [21]. Zhang et al. proposed a dielectric device, made of Veroclear810, consisting of an oracle subblock, two Fourier transform (FT) subblocks, and a phase plate subblock [4,21]. The oracle subblock imprints a spatially phase dependent profile on the incoming wave while the FT subblock and phase plate subblock converts the phase difference for the oracle subblock to amplitude information [21]. Through this device they were able to simulate Grover's Algorithm and show that the number of iterations performed on the device was consistent with the efficiency of the quantum search algorithm.

#495919 https://doi.org/10.1364/OE.495919
Journal © 2023 Received 18 May 2023; revised 19 Jul 2023; accepted 3 Aug 2023; published 21 Aug 2023

Optics EXPRESS

Metamaterials have reached a high degree of maturity and have recently emerged as a new approach for quantum computing. In this context, Wei et al. proposed a quantum searcher of an on-chip silicon device that consisted of four metasurfaces: an oracle metasurface, two metalenses, and a middle metasurface where different spatial positions of the incident wave showed repeatability in the distribution of the output wave intensity [4]. Cheng et al. experimentally verified a Deutsch-Jozsa (DJ) algorithm with a millimeter scaled all-dielectric device [20].

Here, we report a new design for a quantum algorithm emulator in the THz frequency regime based on a simple platform and optimized by machine learning. The investigated device is composed of a microstructured oracle subblock made of silicon substrate and a FT subblock made of Kapton polyimide. The Kapton film chosen acts as a 2D photonic crystal (PhC) slab and proven to exhibit strong electric field confinement and interaction with THz waves with minimal absorption loss [22]. In this work, numerical simulations enhanced by machine learning (ML) were applied to optimize the hole radii and thickness of the FT subblock to achieve an optimal distribution of wave intensities. The structural design of the QAE is first presented along with the numerical analysis showing the initial optimized output. Lastly, the process and results for the ML process are discussed. Our aim is that the simple design of our device and its compact size may strongly relax the constraints for high frequency domains (e.g., IR and visible) which are expected to play a larger role in photonics and quantum technology as a whole.

2. Numerical evaluation of QAE

The block diagram of the QAE is shown in Fig. 1 (top panel). A schematic of the DJ algorithm is shown in Supplement 1, Sec. A. The whole device consists of two functional subblocks, oracle and Fourier transform, respectively, brought into optical contact. Figure 1 (bottom panel) represents the schematic view of the metamaterial-based quantum emulator. The oracle block is made from a 500-μm-thick silicon (Si) substrate. It modulates the electric field profile of the incident THz light by assigning a phase shift of 0 or π on each spatial position along y-axis. This phase shift is introduced by physically varying the radius of the holes array drilled in the silicon substrate, or oracle block, and by consequence also varies the effective electric permittivity ϵ_e along the y-axis thereby encoding the function $f(y)$.

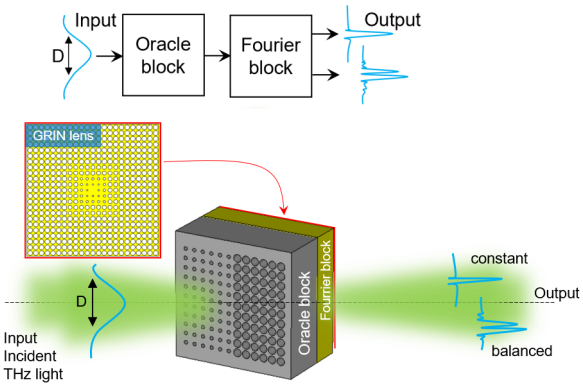

Fig. 1. Schematic of the Quantum Algorithm Emulator. (Top panel) Block diagram of the DJ algorithm and (Bottom panel) metamaterial-based multi-layer configuration of the DJ algorithm emulator. The input THz wave of width D is modulated by the oracle block of varying hole diameters and then transformed through the Fourier block to show the output signal of either a constant function (top output) or balanced function (bottom output).

The Fourier transform block is made from 127-μm-thick polyimide film with various hole sizes acting as an all-dielectric GRIN metalens as shown in Figs. 2(a) and (b). Each hole has a

Optics EXPRESS

period of 70 μm with varying radii of 10, 15, 20, 25, and 30 μm, respectively from the center to the edge of the device. Due to the rotational symmetry imposed by the geometry of the design, the structure has an identical response for both linearly TE-polarized and TM-polarized waves. Also, note that the use of flexible substrates provides an unprecedented route to achieve frequency tunability due to modifications in the profile and the periodicity of the structures when the substrates are manipulated mechanically [22].

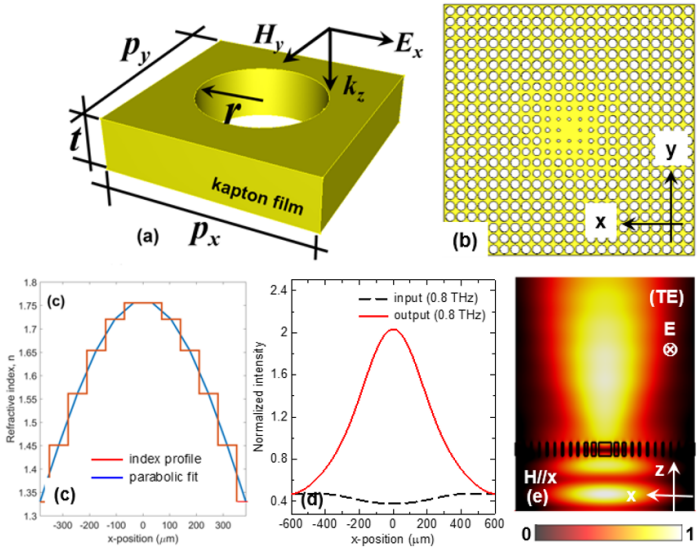

Fig. 2. (a) Structural design of the unit cell with the relevant geometrical dimensions: $p_x = p_y = 70$ μm, $t = 127$ μm and r varies 10, 15, 20, 25 and 30 μm, respectively. (b) Schematic view of the GRIN lens. The aperture size of the lens is ~ 1 mm. (c) Index profile of the structure at 0.8 THz. The blue solid line is a parabolic fit to the refractive index profile. (d) Simulated electric field intensity on the focal plane at 0.8 THz. The input electric field intensity is also plotted for comparison. (e) Simulated normalized electric field distribution of the GRIN lens at 0.8 THz, for linearly TE-polarized radiation.

The polyimide film is treated as a dielectric with $\varepsilon = 3.3 + i0.05$. For the GRIN lens design, we chose a radially symmetric refractive index gradient following a parabolic index profile $n(r) = n_0 \mathrm{sech}(\alpha r)$ with $\alpha = 1/r_0 + \cosh^{-1}(n_0/n_r 0)$ [Fig. 2(c)]. For this purpose, we introduced a spatial variation of the refractive index by arraying unit cells of different radius such that the refractive index gradually decreased from the center of the GRIN lens. The dimensions of each cell are modified to fit the refractive index profile on the device. The design of the final GRIN lens structure is shown in Fig. 2(b). The effective permittivity of the oracle block can be expressed as: $\epsilon_e(y) = (3\lambda_0/d_0)^2$; $\Delta\phi = 0$, $\epsilon_e(y) = (2.5\lambda_0/d_0)^2$; $\Delta\phi = \pi$, where d_0 is the length of the oracle block and λ_0 the working wavelength.

To examine the performance of the designed metalens, we plotted in Fig. 2(d) the cross-section of the normalized intensity profiles in the plane $y = 0$ (axial x–z plane) around the focal point of the metalens at 0.8 THz. The input electric field intensity is also plotted for comparison. Shown in Fig. 2(e) we present the normalized local electric field distribution of the GRIN lens at 0.8 THz, for linearly TE-polarized radiation. In it, we aim to clearly demonstrate the successful realization of the focusing property of our design. When the incident light irradiates the surface of the oracle block, the phase of the transmitted wave is modulated with a factor $k_0 n(y) d_0$, where $k_0 = 2\pi/\lambda_0$ is the vacuum wave vector, d_0 is the thickness of the oracle block and $n(y)$ is the effective refractive index at position (y). The detecting function $f(y)$ is encoded into the input states by assigning a

Optics EXPRESS

phase modulation on each spatial position (y) along the input transversal direction. The refractive index of the oracle operator is designed to achieve either 0 or π phase distribution depending on the value of the function f. The Fourier transform operator is used to evaluate the final results on the output signal. There are optical processes that can produce Fourier transform of field distribution, such as diffraction and Optical spatial filtering, respectively. Generally, the far field diffraction pattern is observed at infinity. By placing a lens after the diffracting aperture, the plane at infinity is imaged onto the focal plane of the lens. This explains why a lens can perform a Fourier transform.

To evaluate the performance of the device, we performed numerical simulations based on the finite-difference time-domain (FDTD) method. The length scale of the mesh was set to be less than or equal to $\lambda_0/10$ throughout the simulation domain, where λ_0 is the central wavelength of the incident radiation. The input and output ports are located at about $10\lambda_0$ from the device with open boundary conditions. The blue line plots in Fig. 3 show the electric field intensity at the focal plane of the GRIN lens with the detecting function being constant and balance, respectively, computed for the initial numerical analysis at 0.8 Thz. The maximum intensity at y = 0 position means the encoded function $f(y)$ is constant. However, if the center intensity is zero this indicates that the oracle subblock carries a balance function. Since the 0 and π phase elements correspond with different effective permittivities, it makes the oracle subblock processes spatially varying impedance which results in different transmissions creating a non-symmetric intensity for the output of the electric field as shown in Fig. 3 (blue line, right panel).

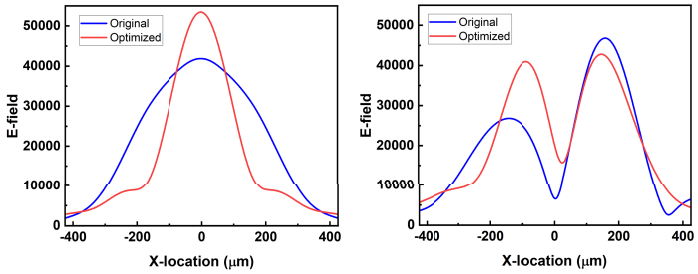

Fig. 3. The electric field intensity at the focal plane of the GRIN lens for an intermediate working frequency of 0.8 THz, with the detecting function being constant (left panel) and balance (right panel), respectively. The blue and red lines are simulations of the output pre-(original) and post-application (optimized) of machine learning based inverse design.

3. Machine learning optimization of QAE

To further engineer the structural parameters, a machine learning (ML) based optimization procedure is implemented into the design of the grin lens. ML is a powerful tool for optimization [23–28] and is expected to be an efficient complementary of electromagnetic wave numerical simulations [29–31]. Recently, one of the most popular ML techniques used in conjunction with EM field wave simulations is the inverse-design model [32–36]. Comparing to conventional methods, inverse-design traces the geometry configurations from the output performance such as resonant frequencies or S-parameters [28,37]. The overall procedure used in this study is shown in Fig. 4. First, the data for training the proposed neural network (NN) model is generated using the numerical simulation software (i.e., CST) based on the initial structure parameters as in Fig. 4(a). After which, the geometry configuration is randomly generated using MATLAB with the constraints on r_i and h, respectively. The constraints for r_i are $0<r_i<a/2$ and $r_1<r_2<r_3<r_4<r_5<r_6$ where $a = 70\ \mu m$ is the characteristic length of the unit cell of each hole in Fig. 4(b). Additionally, the constraint of h is $50\ \mu m<h<300\ \mu m$. To optimize the performance of

Optics EXPRESS

the GRIN lens, we divided the holes on the surface into six groups from inner to outer ring with the radius of r_1, r_2, r_3, r_4, r_5, and r_6, respectively. In addition, the thickness of the grin lens h is also involved into the optimized procedure since the path of the wave's propagation can also affect the performance. Additional details are provided in Supplement 1, Sec. B.

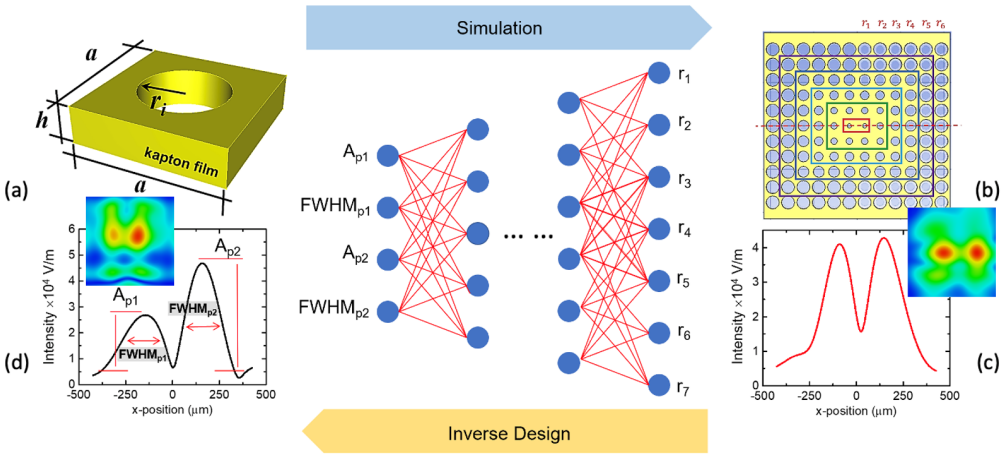

Fig. 4. The schematic of the proposed ML-based inverse-design of the Fourier subblock. (a) Unit cell used for generating the whole GRIN lens with varying hole diameters shown in (b). (c) Result of the balanced function which is used to apply inverse design to best fit the peaks (d) comparing the initial data of amplitude at π and the full width at half maximum (FWHM) of π the two peaks as the input parameters. The focused spot sizes are illustrated in the insets for the initial and optimized device.

According to the Deutsch-Jozsa algorithm, the key point of the design is in fact the performance of the balanced function case since the output of all zero or all one case will absolutely be one peak. It is important that the proposed structure has an ability to distinguish the input status (i.e., constant or balance) from the output performance. Therefore, the proposed optimization procedure mainly focuses on the output spectrum [38,39]. Hence, we only need to optimize the performance of the balanced function shown in Fig. 4(c). Moreover, since the output of the half-zero half-one case is expected to have two peaks on two sides, the input for the inverse design model can be simplified as the features of the peaks. Here, we choose the amplitude A_{pi} and the full width at half maximum (FWHM) $FWHM_{pi}$ of the two peaks as the input parameters, i.e.,

$$(\bar{v}_{in}) = [A_{p1}, FWHM_{p1}, A_{p2}, FWHM_{p2}] \tag{1}$$

where p_1 and p_2 denote the left and right peak, respectively in Fig. 4(d).

The data is then split into the training and validating set with the ratio of 80% – 20%. The training set is used to train the proposed NN model, while the validating set is used to check the performance of the model after each training round. Since the length of the input and output vectors are four and seven only, the artificial neural network (ANN) is well enough to achieve the optimal design. There are seven hidden layers in the proposed ANN model, each hidden layer has 16, 16, 32, 32, 16, 16, and 7 channels, respectively. All the layers except for the last one come with a rectified linear activation function (ReLU). The channel in the last layer is the output of the NN model representing the geometry configuration from Fig. 3 which is represented in the following equation:

$$(\bar{v}_{out}) = [r_1, r_2, r_3, r_4, r_5, r_6, h] \tag{2}$$

where $r_1, r_2, r_3, r_4, r_5, r_6$ denote the radii of the six layers and h is the thickness of the GRIN lens.

Optics EXPRESS

After training with 100 iterations, the proposed model can precisely predict the geometry configuration from ($\bar{v}_{out}$). Hence, we can feed the model with the desired ($\bar{v}_{in}$) so that the desired optimal geometry configuration ($\bar{v}_{out}$) is achieved. However, if the values of ($\bar{v}_{in}$) exceed the performance limitation of the proposed GRIN lens, ($\bar{v}_{out}$) may not get the same performance as ($\bar{v}_{in}$). As a result, it is required to re-validate the connection between ($\bar{v}_{in}$) and ($\bar{v}_{out}$) via the numerical simulation software. After several trials, an optimal geometry configuration is achieved and validated by FDTD method. According to Fig. 3, the performance with respect to the output spectral balance is much better for the inverse-design than the initial design. The detail comparison of the initial and optimal design is represented in Table 1.

Table 1. Top: Comparison of initial numerical GRIN lens parameters to the machine Learning optimized parameters. Bottom: The performance comparison of the initial and optimal design for (i) all-zero all-one case and (ii) half-zero half one case as represented by the output wave characteristics.

Parameter	r_1	r_2	r_3	r_4	r_5	r_6	h
Initial	10	15	25	25	30	30	127
Optimal	11.97	16.09	21.24	27.88	31.59	34.91	289.86

Case	All zero / All one		Half-zero half-one			
Parameter	Ap	FWHM	Ap_1	$FWHM_1$	Ap_2	$FWHM_2$
Initial	41.872	449.96	26.795	264.50	46.813	208.50
Optimal	53.455	218.15	40.976	195.16	42.792	217.25

From Table 1, the optimized design of the GRIN lens shows minimal increases of all radii except r_3 with changes being no more than 15%. However, the biggest change occurred with a factor of two increase of the thickness. This means the radii sizes were near optimal from the initial numerical analysis and that the amount of the computational metamaterial interacting with the incident wave is crucial in achieving the best output amplitudes and full width half maximum (FWHM) for both cases. The thickness of the GRIN lens needs to be at least one-working wavelength in such a way that the wave can better interact with the medium. The thicker the medium the better the interaction will be. However, if the GRIN lens is too thick, the focal point may fall inside the GRIN lens.

For the constant function case the amplitude has been increased by about 26 % and the FWHM has been decreased by 52%. For the balanced function, the first peak had its amplitude increased by 50% and its FWHM decreased by 26% while the second peak was already close to optimal. Knowing that the efficiency of this method is proportional to the ratio the FWHM of the incoming and outgoing waves [21] we can see from the spectral improvements that the optimization enhanced the device. For the output of either balanced or constant functions, the sharper peaks (higher amplitude and smaller FWHM) mean greater distribution of the wave intensity, stronger focus of the outgoing wave, and a better probability of handling a higher number of database inputs [4,21] as shown in bottom right of Fig. 4 and in the red plot of the right panel of Fig. 3. Cheng et al. also showed an enhancement of their balance function through increasing the number of phase elements in their oracle block.[20] Our design makes the fabrication process simpler for this improvement in output in that we only have to manufacture a thicker GRIN lens.

4. Conclusion

To summarize, we designed, with machine learning, an optimized all-dielectric metadevice as a part of a quantum algorithm emulator for simulating the DJ algorithm in the THz region. Initial structural optimization was constructed using numerical analysis based on FDTD to evaluate its initial performance. Using a ML-based optimization procedure, the original design of the structure was further engineered for an enhanced performance as shown by the two-fold increase in the thickness of the GRIN lens. The resultant optimization showed performance improvements

Optics EXPRESS

in the amplitude and FWHM of the peaks for both the balanced and constant cases and shows promise for the emulation of quantum algorithms with current THz technologies.

Funding. US Department of Energy Office of Science, National Quantum Information Science Research Centers, Co-design Center for Quantum Advantage (C2QA) under Contract No. (DE-SC0012704).

Acknowledgment. Work by UIC was supported in part by U.S. Department of Energy, Office of Science, National Quantum Information Science Research Centers, Co-design Center for Quantum Advantage (C2QA) under Contract No. DE-SC0012704. A. N. B. would like to thank the partial financial support of the GEM Fellowship for this work. Further, Z. A. C. would like to thank the Bridge-to-Faculty Fellowship.

Disclosures. The authors declare no conflicts of interest.

Data availability. Data underlying the results presented in this paper are not publicly available at this time but may be obtained from the authors upon reasonable request.

Supplemental document. See Supplement 1 for supporting content.

References

1. A. C. Arsenault, S. Fournier-Bidoz, B. D. Hatton, H. Míguez, N. Tétreault, E. Vekris, S. H. Wong, S. M. Yang, V. Kitaev, and G. A. Ozin, "Towards the synthetic all-optical computer: science fiction or reality?" J. Mater. Chem. **14**(5), 781–794 (2004).
2. J. Touch, A.-H. Badawy, and V. Sorger, "Optical computing," Nanophotonics **6**(3), 503–505 (2017).
3. J. L. O'Brien, "Optical quantum computing," Science **318**(5856), 1567–1570 (2007).
4. Z. Wei, H. Li, L. Dou, L. Xie, Z. Wang, and X. Cheng, "Metasurface-based quantum searcher on a silicon-on-insulator chip," Micromachines **13**(8), 1204 (2022).
5. N. Yu, P. Genevet, M. A. Kats, F. Aieta, J. Tetienne, F. Capasso, and Z. Gaburro, "Light propagation with phase discontinuities: Generalized laws of reflection and refraction," Science **334**(6054), 333–337 (2011).
6. T. He, T. Liu, S. Xiao, Z. Wei, L. Z. Zhanshan Wang, and X. Cheng, "Perfect anomalous reflectors at optical frequencies," Sci. Adv. **8**(9), 1 (2022).
7. J. Xiang, Z. Tao, X. Li, Y. Zhao, Y. He, X. Guo, and Y. Su, "Metamaterial-enabled arbitrary on-chip spatial mode manipulation," Light: Sci. Appl. **11**(1), 168 (2022).
8. P. Stellman, K. Tian, and G. Barbastathis, "Design of gradient index (grin) lens using photonic non-crystals," *2007 Quantum Electronics and Laser Science Conference* pp. 1–2 (2007).
9. D. Headland, W. Withayachumnankul, M. Webb, and D. Abbott, "Beam deflection lens at terahertz frequencies using a hole lattice metamaterial," in *2013 38th International Conference on Infrared, Millimeter, and Terahertz Waves (IRMMW-THz)*, (IEEE, 2013), pp. 1–2.
10. W. Bai, P. Yang, J. Huang, D. Chen, J. Zhang, Z. Zhang, J. Yang, and B. Xu, "Near-infrared tunable metalens based on phase change material ge2se2te5," Sci. Rep. **9**(1), 5368 (2019).
11. F. Gaufillet, S. Marcellin, and E. Akmansoy, "Dielectric metamaterial-based gradient index lens in the terahertz frequency range," IEEE J. Sel. Top. Quantum Electron. **23**(4), 1–5 (2017).
12. A. I. Hernandez-Serrano, R. Mendis, K. S. Reichel, W. Zhang, E. Castro-Camus, and D. M. Mittleman, "Artificial dielectric stepped-refractive-index lens for the terahertz region.," Opt. Express **26**(3), 3702–3708 (2018).
13. Q. Yang, J. Gu, D. Wang, X. Zhang, Z. Tian, C. Ouyang, R. Singh, J. Han, and W. Zhang, "Efficient flat metasurface lens for terahertz imaging," Opt. Express **22**(21), 25931–25939 (2014).
14. O. Paul, B. Reinhard, B. Krolla, R. Beigang, and M. Rahm, "Gradient index metamaterial based on slot elements," Appl. Phys. Lett. **96**(24), 241110 (2010).
15. M. F. Volk, B. Reinhard, J. Neu, R. Beigang, and M. Rahm, "In-plane focusing of terahertz surface waves on a gradient index metamaterial film," Opt. Lett. **38**(12), 2156–2158 (2013).
16. J. Neu, B. Krolla, O. Paul, B. Reinhard, R. Beigang, and M. Rahm, "Metamaterial-based gradient index lens with strong focusing in the thz frequency range," Opt. Express **18**(26), 27748–27757 (2010).
17. C. Zeng, X. Liu, and G. Wang, "Electrically tunable graphene plasmonic quasicrystal metasurfaces for transformation optics," Sci. Rep. **4**(1), 5763 (2014).
18. M. Maasch, M. Roig, C. Damm, and R. Jakoby, "Voltage-tunable artificial gradient-index lens based on a liquid crystal loaded fishnet metamaterial," Antennas Wirel. Propag. Lett. **13**, 1581–1584 (2014).
19. F. Moharrami and Z. Atlasbaf, "Tunable grin lensing based on graphene-dielectric multilayer metamaterials," J. Opt. **22**(2), 025102 (2020).
20. K. Cheng, W. Zhang, Z. Wei, Y. Fan, C. Xu, C. Wu, X. Zhang, and H. Li, "Simulate deutsch-jozsa algorithm with metamaterials," Opt. Express **28**(11), 16230–16243 (2020).
21. W. Zhang, K. Cheng, C. Wu, Y. Wang, H. Li, and X. Zhang, "Implementing quantum search algorithm with metamaterials," Adv. Mater. **30**(1), 1703986 (2018).
22. C. Kyaw, R. Yahiaoui, Z. A. Chase, V. N. H. Tran, A. Baydin, F. Tay, J. Kono, M. Manjappa, R. Singh, D. C. Abeysinghe, A. M. Urbas, and T. A. Searles, "Guided-mode resonances in flexible 2d terahertz photonic crystals," Optica, **7**, 537 (2020).

Optics EXPRESS

23. R. Zaheer and H. Shaziya, "A study of the optimization algorithms in deep learning," *Third International Conference on Inventive System and Control (ICISC)* (2019).
24. S. K. Patel, J. Surve, J. Parmar, A. Natesan, and V. Katkar, "Graphene-based metasurface refractive index biosensor for hemoglobin detection: Machine learning assisted optimization," IEEE Transactions on Nanobioscience (2022).
25. S. Koziel and M. Abdullah, "Machine-learning-powered em-based framework for efficient and reliable design of low scattering metasurfaces," IEEE Trans. Microwave Theory Techn. **69**(4), 2028–2041 (2021).
26. N. Shlezinger, Y. C. Eldar, and S. P. Boyd, "Model-based deep learning: On the intersection of deep learning and optimization," IEEE Access **10**, 115384–115398 (2022).
27. S. An, C. Fowler, B. Zheng, M. Y. Shalaginov, H. Tang, H. Li, L. Zhou, J. Ding, A. M. Agarwal, C. Rivero-Baleine, K. A. Richardson, T. Gu, J. Hu, and H. Zhang, "A deep learning approach for objective-driven all-dielectric metasurface design," ACS Photonics **6**(12), 3196–3207 (2019).
28. W. Ma, Z. Liu, Z. A. Kudyshev, A. Boltasseva, W. Cai, and Y. Liu, "Deep learning for the design of photonic structures," Nat. Photonics **15**(2), 77–90 (2021).
29. W. Ma, F. Cheng, Y. Xu, Q. Wen, and Y. Liu, "Probabilistic representation and inverse design of metamaterials based on a deep generative model with semi-supervised learning strategy," Adv. Mater. **31**(35), 1901111 (2019).
30. W. Huang, Z. Wei, B. Tan, S. Yin, and W. Zhang, "Inverse engineering of electromagnetically induced transparency in terahertz metamaterial via deep learning," J. Phys. D: Appl. Phys. **54**(13), 135102 (2021).
31. X. Zhou, Q. Xiao, and H. Wang, "Metamaterials design method based on deep learning database," in *Journal of Physics: Conference Series*, vol. 2185 (IOP Publishing, 2022), p. 012023.
32. M. Sedaghat, R. Trinchero, Z. H. Firouzeh, and F. G. Canavero, "Compressed machine learning-based inverse model for design optimization of microwave components," IEEE Trans. Microwave Theory Tech. **70**(7), 3415–3427 (2022).
33. Z. Li, R. Pestourie, Z. Lin, S. G. Johnson, and F. Capasso, "Empowering metasurfaces with inverse design: Principles and applications," ACS Photonics **9**(7), 2178–2192 (2022).
34. W. Wang, J. Huang, H. Ouassal, and J. Chisum, "Inverse grin lens design using artificial neural network and geometrical optics," 2022 IEEE International Symposium on Antennas and Propagation and USNC-URSI Radio Science Meeting (AP-S/URSI) pp. 1–2 (2022).
35. D. Erricolo, P.-Y. Chen, A. Rozhkova, E. Torabi, H. Bagci, A. Shamim, and X. Zhang, "Machine learning in electromagnetics: A review and some perspectives for future research," *2019 International Conference on Electromagnetics in Advanced Applications (ICEAA)* pp. 1377–1380 (2019).
36. M. V. Zhelyeznyakov, S. Brunton, and A. Majumdar, "Deep learning to accelerate scatterer-to-field mapping for inverse design of dielectric metasurfaces," ACS Photonics **8**(2), 481–488 (2021).
37. Z. Liu, D. Zhu, S. P. Rodrigues, K.-T. Lee, and W. Cai, "Generative model for the inverse design of metasurfaces," Nano Lett. **18**(10), 6570–6576 (2018).
38. S. Lloyd, M. Mohseni, and P. Rebentrost, "Quantum algorithms for supervised and unsupervised machine learning," arXiv, arXiv:1307.0411v2 (2013).
39. L. Cincio, Y. Subasi, A. T. Sornborger, and P. J. Coles, "Learning the quantum algorithm for state overlap," New J. Phys. **20**(11), 113022 (2018).